Effect of Initial Iron Content in a Zinc Bath on the Dissolution Rate of Iron During a Hot Dip Galvanizing Process

SANG MYUNG LEE, SUK KYU LEE, DOO-JIN PAIK, and JOO HYUN PARK

The mechanism of iron dissolution and the effect of initial Fe content in a Zn bath on the dissolution rate of iron were investigated using a finger rotating method (FRM). When the initial iron content, [Fe]°, in the zinc bath was less than the solubility limit, the iron content in the zinc bath showed a rapid increase, whereas a moderate increase was observed when [Fe]° was close to the solubility limit. Based on Eisenberg's kinetic model, the mass transfer coefficient of iron in the present experimental condition was calculated to be $k_M = 1.2 \times 10^{-5}$ m/s, which was similar to the results derived by Giorgi *et al.* under industrial practice conditions. A dissolution of iron occurred even when the initial iron content in the zinc bath was greater than the solubility limit, which was explained by the interfacial thermodynamics in conjunction with the morphology of the surface coating layer. By analyzing the diffraction patterns using TEM, the outermost dendritic-structured coating layer was confirmed as $FeZn_{13}$ (ζ). In order to satisfy the local equilibrium based on the Gibbs–Thomson equation, iron in the dendrite-structured phase spontaneously dissolved into the zinc bath, resulting in the enrichment of iron in front of the dendrite tip. Through the diffusion boundary layer in front of the dendritic-structured layer, dissolved Fe atoms diffused out and reacted with Zn and small amounts of Al, resulting in the formation of dross particles such as $FeZn_{10}Al_x$ (δ). It was experimentally confirmed that the smaller the difference between the initial iron content in the zinc bath and the iron solubility limit at a given temperature, the lower the number of formed dross particles.

DOI: 10.1007/s11661-017-3966-4

I. INTRODUCTION

DURING the hot dip galvanizing process, dross particles, which are intermetallic compounds of the Zn-Fe-Al system, affect the surface quality of the steel sheet. Thus, the changes in Fe or Al concentration in molten zinc have a significant impact on the production of high-quality steels. When a steel sheet is immersed in a zinc bath, dissolved iron creates the Fe-Zn and Fe-Al intermetallic compound layer on the surface of the steel sheet.[1,2] Additionally, dissolved iron from the steel sheet promotes the precipitation of δ ($FeZn_{10}Al_x$), ζ ($FeZn_{13}$), and η ($Fe_2Al_5Zn_x$) phase dross particles in molten zinc.

The bulk of research with respect to the dross in molten zinc are based on thermodynamics and phase equilibria for the Zn-Al-Fe system by employing experimental and/or computational methodologies. In the modeling work of Nakano *et al.*,[3] the Zn-Al-Fe phase diagram (Zn-rich corner) was evaluated at full equilibrium from 693 K to 773 K (420 °C to 500 °C). In the modeling work of McDermid *et al.*,[4] solubility measurements and thermodynamic modeling were performed to depict the zinc-rich corner of the Zn-Al-Fe phase diagram. Park *et al.*[5] recently determined that the addition of Al into the Zn-Fe melt provided local supersaturation and depletion of Al content, resulting in the nucleation and growth of both $Fe_2Al_5Zn_x$ and $FeZn_{13}$. However, Al was continuously homogenized as the reaction proceeded, and thus a very fine and stable $FeZn_{10}Al_x$ phase formed after 30 minutes.

Alternatively, dross is generated due to the dissolution of iron from the steel sheet. Therefore, the kinetic study on the dissolution of iron is highly important. In the kinetic modeling work by Giorgi *et al.*,[6] the mass transfer coefficient of iron k_M was taken as 1.7×10^{-5} m/s when iron was saturated in molten zinc at 733 K (460 °C). Michal *et al.*[7–9] predicted the value of k_M using Fick's second law with the appropriate boundary condition derived from the iron concentration in the liquid zinc from Liu and Tang's model and Toussaint *et al.*'s model.[7–9] The mass transfer coefficients previously reported are listed in Table I.

Michal *et al.*[7] also found that the k_M increased only slightly as the strip line speed increased and followed an Arrhenius relationship with the reciprocal of the strip

SANG MYUNG LEE and JOO HYUN PARK are with the Department of Materials Engineering, Hanyang University, Ansan 426-791, Korea. Contact e-mail: basicity@hanyang.ac.kr SUK KYU LEE is with the Technical Research Center, POSCO, Gwangyang 545-711, Korea. DOO-JIN PAIK is with the Surface Treatment Plant I, Surface Treatment Department, POSCO, Gwangyang 545-711, Korea.
Manuscript submitted August 12, 2016.
Article published online January 17, 2017

entry temperature. They also reported that an increase in Al concentration from 0.118 to 0.124 mass pct in the Zn bath caused a slight decrease in k_M because the inhibition layer formed rapidly in a high Al content condition in the zinc bath. This inhibition layer reduces iron dissolution from steel. Additionally, the diffusion coefficient of iron in the Zn-0.05 pct Al-0.003 pct Fe melt was measured using the rotating disk technique by Giorgi *et al.*[11]

Even though previous studies have predicted the dissolution rate of Fe in practical conditions, the mechanism of iron dissolution from the steel sheet has not been fully clarified. Thus, the objective of the present work was to confirm the mechanism of iron dissolution as well as the effect of the initial Fe content in the Zn bath on the dissolution rate of iron using a finger rotating method (FRM), in which the iron cylinder was rotated with a fixed revolution per minute (rpm) rather than a simple dipping method in order to qualitatively simulate the dynamic galvanizing operation conditions.

II. EXPERIMENTAL

A. *Materials Preparation*

High-purity iron (99.99 pct) was manufactured into a cylindrical shape with dimensions of 10 mm in diameter and 60 mm in height. The Zn-Fe-Al bath was prepared with the initial content of 200, 240, and 300 mass ppm Fe, respectively, and the Al content was 0.13 mass pct in all experiments.

Table I. Mass Transfer Coefficients Derived Under Various Conditions

k_M (m/s)	Temperature [K (°C)]	Immersion time (s)	Authors (Ref)
1.7×10^{-5}	733 (460)	2.0	Giorgi *et al.*[6]
2.4×10^{-4}	723 (450)	0.04	Liu and Tang[8]
3.5×10^{-6}	733 (460)	0.1	Toussaint *et al.*[9]
8.3×10^{-6}	753 (480)	0.1	Toussaint *et al.*[9]
1.0×10^{-6}	743 (470)	0.5	Tang[10]
1.2×10^{-5}	728 (455)	—	present study

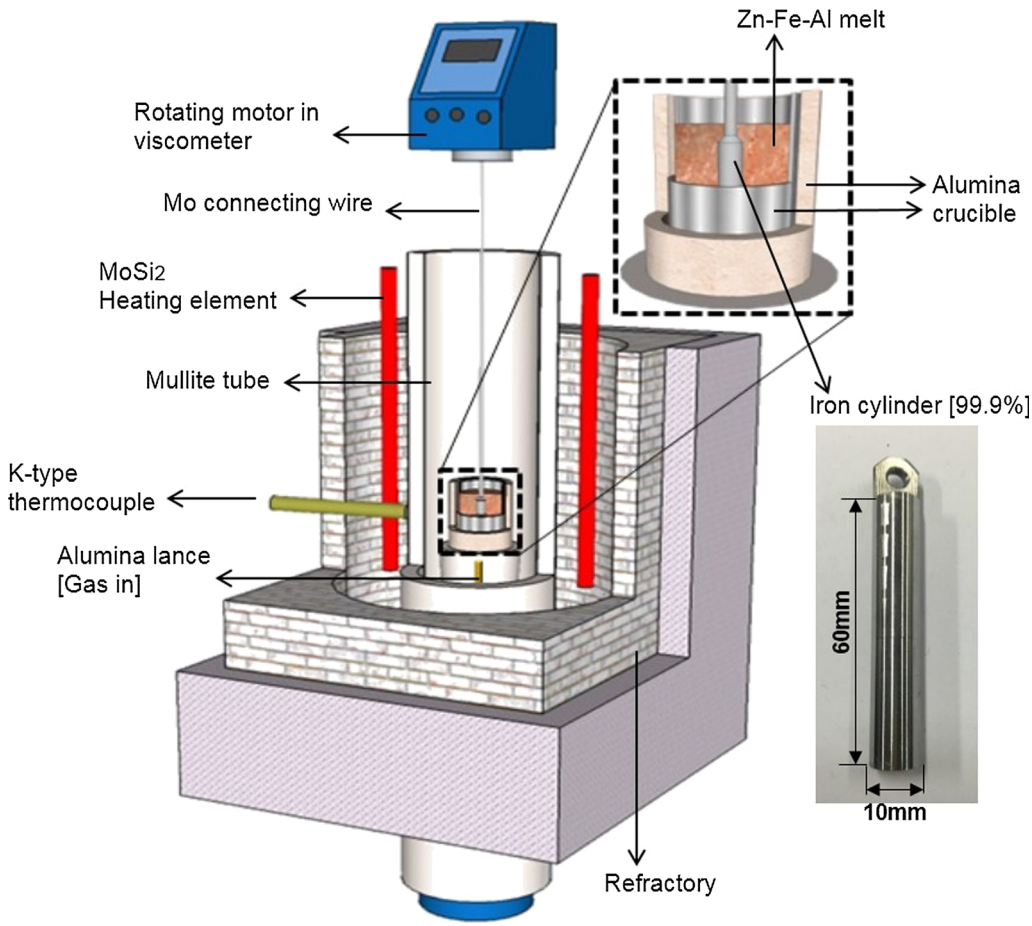

Fig. 1—Schematic diagram of the experimental apparatus.

B. *Finger Rotating Method (FRM)*

The experimental apparatus used in the present study is schematically shown in Figure 1. The Zn-Al-Fe alloy (400 g) was loaded in a fused alumina crucible (diameter 45 mm, height 65 mm), which was heated and maintained at 773 K (500 °C) for 1 hour and slowly cooled to 728 K (455 °C). The alloy was maintained for 1 hour at 728 K (455 °C) for homogenization in a vertical electric resistance furnace under an Ar gas atmosphere, which was purified by passing the gas through a Mg turning furnace at 723 K (450 °C). The iron cylinder was connected to a rotating motor (150 rpm) equipped in a viscometer (Brookfield model LV-DV II+ Pro). To observe the Fe dissolution, iron rod was rotated for 90, 180, and 360 minutes. Bath samples were taken 10 mm from the bottom of the crucible by a vacuum suction method.

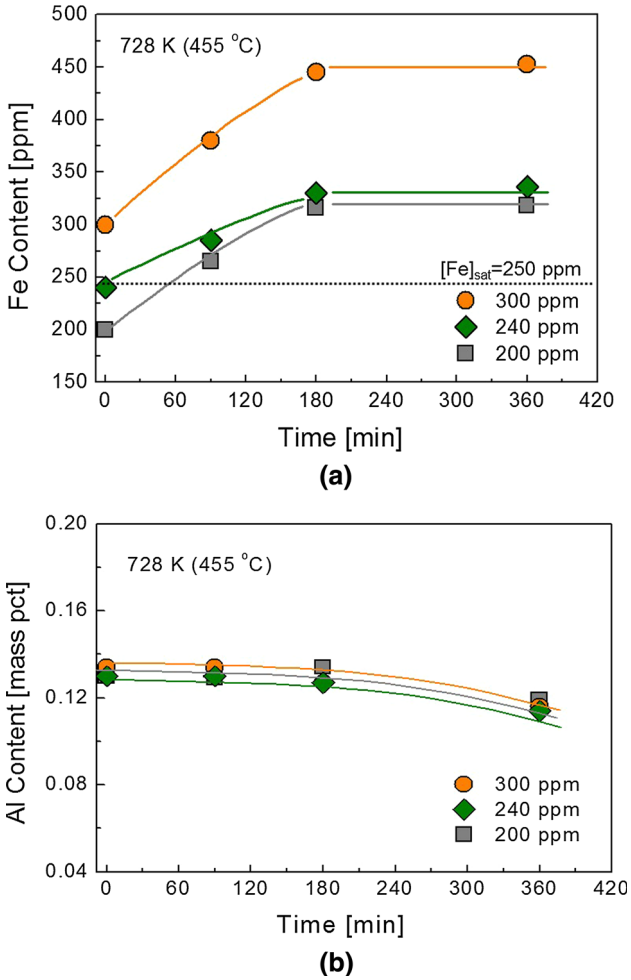

Fig. 2—Variation of Fe (*a*) and Al (*b*) content in the zinc bath as a function of rotating time at 728 K (455 °C).

C. *Analysis Technique*

The bath samples were prepared for chemical analysis by an inductively coupled plasma-atomic emission spectrometry (ICP-AES; Spectro model Spectro Arcos). The dross phase and surface morphology of the iron cylinder were analyzed by a field emission scanning electron microscope (FESEM; TESCAN model MIRA3) with an energy-dispersive X-ray spectroscope (EDS) at an operating voltage of 15 kV. The resin-mounted samples were polished using a 0.05 μm colloidal silica suspension.

For phase identification of an interfacial product layer and the dross particles, a transmission electron microscope (TEM; JEOL JEM-2010) was used at an operating voltage of 200 kV. The TEM sample was prepared by the *in situ* lift out technique, which consists of extracting and transferring a small rectangular-shaped thin film to a TEM grid in a focused ion beam (FIB) chamber. Phase identification was performed by comparing diffraction patterns with the results of Hong *et al.*[12]

III. RESULTS AND DISCUSSION

A. *Kinetics of Iron Dissolution from a Cylinder-Shaped Sample*

The changes in the content of Fe and Al in molten zinc as a function of rotating time are shown in Figure 2. In all experiments, the Fe content increased very rapidly, whereas the Al content decreased slowly with reaction time. The solubility limit of Fe in the galvanizing bath was calculated by Eq. [1], which was suggested by McDermid *et al.*[4]

$$\ln\left[(\text{mass pct Fe})^2\ (\text{mass pct Al})\right] = 24.7052 - \frac{24,871.08}{T}. \quad [1]$$

From Eq. [1], the saturation limit of Fe in molten zinc containing 0.13 mass pct Al was calculated to be 250

Table II. Physical Data for the Calculation of the Mass Transfer Coefficient

Symbol	Value	Unit	Notation
k_M	1.2×10^{-5}	m/s	mass transfer coefficient
v	5.45×10^{-7}	m^2/s	kinematic viscosity
U	6.3×10^{-2}	m/s	periphery velocity of the Fe cylinder
d	1.0×10^{-2}	m	diameter of the Fe cylinder
D	1.18×10^{-9}	m^2/s	diffusion coefficient of Fe in Zn
Re	1153	—	Reynolds number
Sc	462	—	Schmidt number

mass ppm at 728 K (455 °C), indicating that the iron-containing dross particles can be precipitated when the Fe content in the zinc bath is greater than 250 mass ppm at 728 K (455 °C). Thus, from the results shown in Figure 2, large amounts of dross particles were precipitated in the 180 and 360 min samples. In all conditions, the iron content increased until 180 min, followed by a constant value. When the initial iron content, [Fe]°, in the zinc bath was 240 mass ppm, the iron content in the zinc bath increase at a moderate rate of 0.53 ppm Fe/min, whereas the relatively rapid increase (0.71 ppm Fe/min) was observed when [Fe]° = 200 mass ppm. In contrast, the Al content was reduced slightly. A decrease in Al content possibly originated from the formation of dross particles.

The dissolution flux of iron (J) from the cylindrical shape in liquid zinc can be quantitatively analyzed by Eq. [2] with the mass transfer coefficient formula, called the Eisenberg equation, given in Eq. [3]:[13,14]

$$J = k_{\mathrm{M}}(C_{\mathrm{sat}} - C_{\mathrm{m}}) \qquad [2]$$

$$k_{\mathrm{M}} = 0.079 Re^{-0.33} Sc^{-0.66} U \left(Re = \frac{Ud}{v}, Sc = \frac{v}{D} \right), \qquad [3]$$

where k_{M}, v, U, d, D, C_{sat}, and C_{m} are the mass transfer coefficient of iron (m/s), kinematic viscosity of the melt (m^2/s), periphery velocity of the iron cylinder (m/s), diameter of the iron cylinder (m), diffusion coefficient of iron in molten zinc (m^2/s),[11] saturation content, and initial content of Fe in molten zinc (mol/m^3), respectively. Re is the Reynolds number, and Sc is the Schmidt number. The mass transfer coefficient of iron (k_{M}) in the present experimental condition was calculated to be 1.2×10^{-5} m/s from Eq. [3], *i.e.*, $Re = 1153$, $Sc = 462$, and $U = 0.063$ m/s.[14] The specific physical properties are listed in Table II. The k_{m} value derived in the present study is similar to the result of Giorgi *et al.*[6] Thus, it is reasonable to estimate the dissolution rate of iron by accepting the present mass transfer coefficient in the kinetic analysis.

When [Fe]° = 200 and 240 mass ppm, a dissolution flux J was estimated to be 6.9×10^{-5} and 1.4×10^{-5} mol/m^2s, respectively, because of the difference in driving force, *viz.* (C_{sat}–C_{m}), the dissolution flux J in the [Fe]° = 200 mass ppm melt was greater than that in the [Fe]° = 240 mass ppm melt. Thus, the increasing tendency of Fe content in the zinc bath observed in Figure 2 was quite reasonable. Even though the initial Fe content in the zinc bath (0.003 mass pct) was much less than the saturation limit (0.032 mass pct) in Giorgi *et al.*'s study,[11] the dissolution rate of Fe was less than that obtained in the present study. This possibly originated from the fact that the reaction area of the

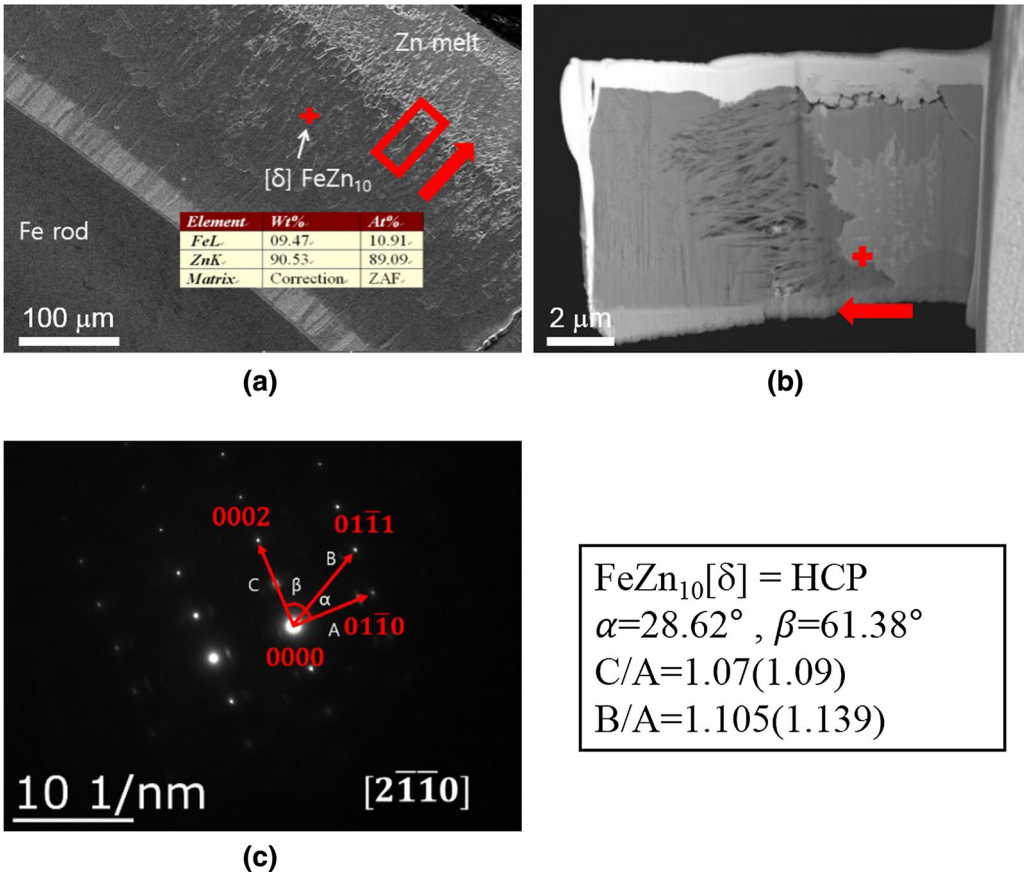

Fig. 3—(*a*) SEM image of the $FeZn_{10}$ layer formed at the surface of the iron cylinder in the system of [Fe]° = 300 ppm at 360 min, (*b*) FIB sample of the squared position in '(a),' and (*c*) diffraction pattern of the cross bar position in '(b).'.

cylinder-shaped sample employed in the present study was greater than that of the disk-shaped sample used in Giorgi *et al.*'s study.

It is interesting in Figure 2 that dissolution of iron occurred even though the initial Fe content in the zinc bath ($[Fe]^{o} = 300$ mass ppm) was greater than the saturation limit (250 mass ppm), which cannot be easily explained by conventional first-order reaction kinetics in the bulk phase described above. Hence, it is necessary to quantitatively characterize the morphology and crystallographic structure of the reaction product coating layer at the surface of the iron cylinder. A more detailed analysis will be given in the following sections.

B. *Characterization (Phase Identification) of the Surface Product Layers*

The SEM image of the iron cylinder cross section is shown in Figure 3(a). A dendrite-structured layer was formed at the outer surface of the $FeZn_{10}$ (δ) phase.[15] Figure 3(b) is a sample image prepared by FIB sectioning for the part appearing in the square in Figure 3(a). Figure 3(c) is a diffraction pattern for the part appearing in the cross bar (in light gray area) in Figure 3(b). The $FeZn_{10}$ (δ) and dendrite-structured layers were clearly separated. The angles of α and β in the $FeZn_{10}$ (δ) layer are 28.62 and 61.38 deg in the SAED pattern, respectively, which corresponds to the HCP $[2\bar{1}\bar{1}0]$ zone.

Diffraction patterns of the outermost dendrite coating layer are shown in Figure 4. Figure 4(a) is a TEM sample image prepared by FIB sectioning and the diffraction patterns of various directions are shown in Figures 4(b) through (d). By analyzing the diffraction patterns in each direction based on Hong *et al.*'s TEM study,[12] the outermost dendritic-structured coating layer, which was formed above the $FeZn_{10}$ (δ) layer in Figure 3, was confirmed as monoclinic $FeZn_{13}$ (ζ). Thus, with the crystallographic information mentioned above,

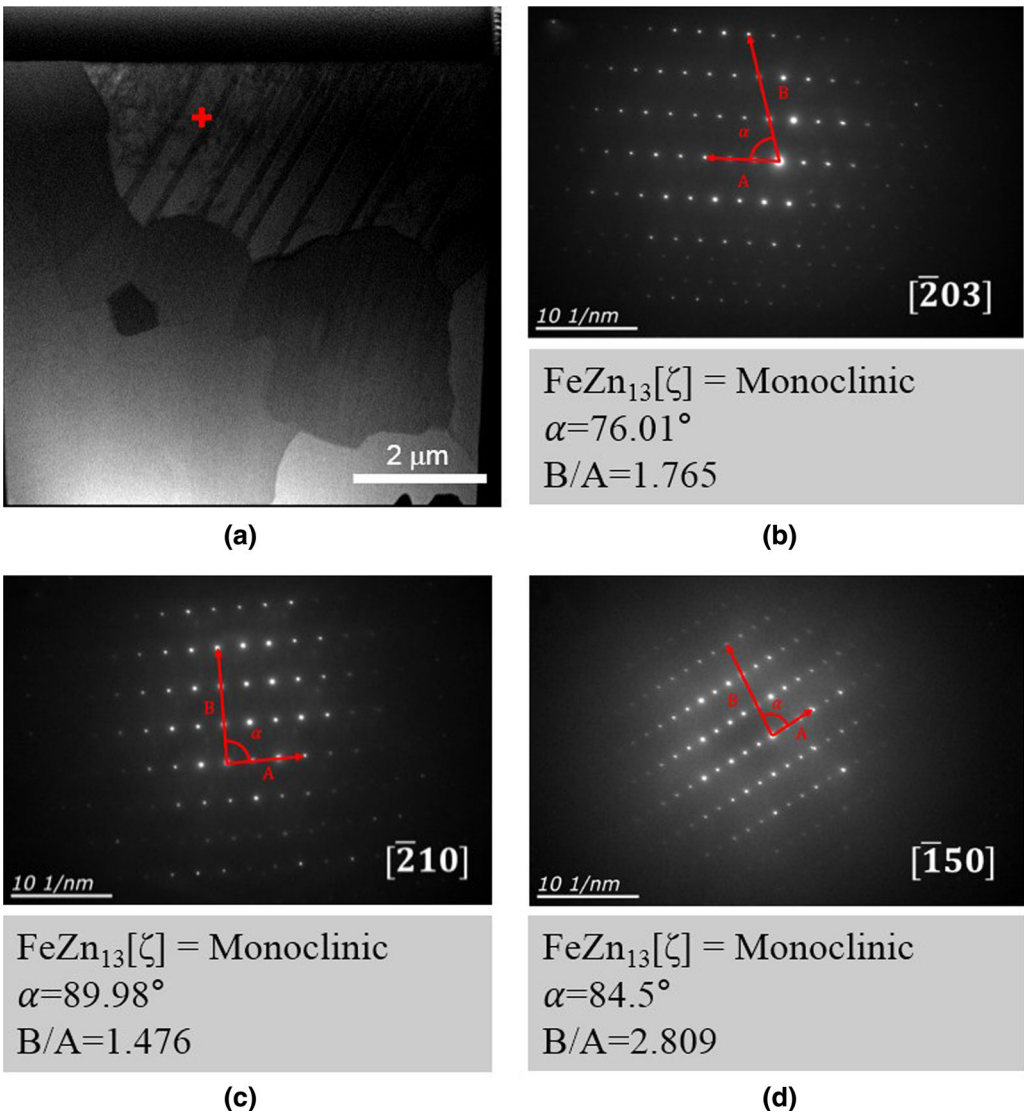

Fig. 4—(*a*) FIB sample image of the $FeZn_{13}$ (ζ) dendrite layer formed at the surface of the iron cylinder in the system of $[Fe]^{\circ}$ = 300 ppm at 360 min and (*b*) to (*d*) diffraction pattern of the cross bar position in '(a).'.

the quantitative analysis for the influence of the dendrite-structured morphology of $FeZn_{13}$ (ζ) layer on the Fe solubility in the Zn bath will be discussed in the following section.

C. *Effect of the Dendritic Morphology of the Product Layer on Iron Solubility in the Sample Vicinity*

If the dendritic structure, which has a sharp tip radius, is formed at the outermost product layer, the solubility limit of iron in the vicinity of the tip face will be increased based on the Gibbs–Thomson equation as follows:[16]

$$\log X^r = \frac{V}{2.3RT} \cdot \frac{2\gamma}{r} + \log X^{\infty}, \qquad [4]$$

where X^r, X^{∞}, V, R, T, r, and γ are, respectively, the solubility of iron in the zinc melt when the radius curvature is r, the solubility of iron when the radius curvature is '∞ (planar condition)', the molar volume of $FeZn_{13}$ (ζ), gas constant, temperature, the radius curvature, and the surface energy of $FeZn_{13}$ (ζ). In order to accomplish local equilibrium between the dendritic structure and liquid co-existing zone, the chemical potential of Fe in the dendrite and zinc bath should be equal.

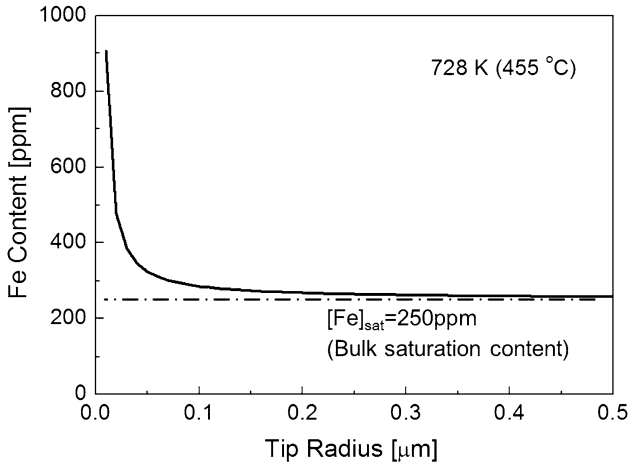

Fig. 5—Variation of Fe solubility as a function of dendrite tip radius at the iron surface calculated from the Gibbs–Thomson effect.

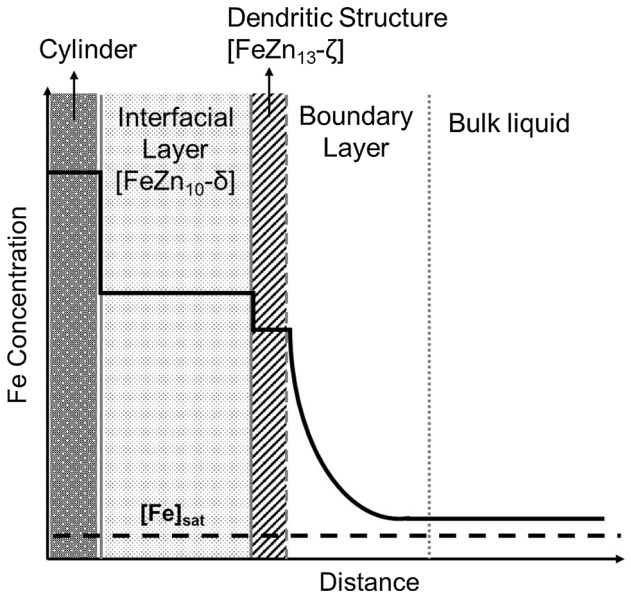

Fig. 6—Schematic diagram of the concentration profile of iron from the iron cylinder side to the bulk zinc melt.

According to Eq. [4], the smaller the radius of curvature, the higher the solubility of iron in front of the iron sample is predicted. Thus, a Fe supersaturation zone could exist in front of the outermost dendrite-structured coating layer.[16] The effect of the dendrite tip curvature on the variation of the local iron solubility calculated from Eq. [4] is shown in Figure 5. It was qualitatively determined that the iron solubility in front of the dendrite tip can be 290 ppm and 330 ppm when the tip radius is 0.1 and 0.05 μm, respectively. These values are greater than the solubility limit of iron (250 ppm) in the bulk phase with an infinity tip radius.

In order to satisfy the local equilibrium, iron in the dendrite-structured phase spontaneously dissolves into a zinc bath, resulting in the enrichment of iron in front of the dendrite tip. The enriched iron atoms can diffuse out from the interface to the bulk zinc melt to form dross particles. Michal *et al.*[7] postulated that iron directly dissolved from the steel sheet into the zinc melt at a very initial stage, *e.g.*, until 0.1 second, with no surface inhibition layer. However, after 0.1 second, iron dissolution occurred through the inhibition layer, which is qualitatively in good correspondence to the present results.

A schematic diagram of the concentration profile of iron from the center of the cylinder to the bulk zinc melt is shown in Figure 6. A diffusion boundary layer may exist in front of the dendritic-structured layer, through which dissolved iron atoms diffuse from the interface into a zinc bath due to the concentration gradient of iron. Thus, iron dissolution could occur even though the initial iron content in the bulk zinc bath was already over the solubility limit at a given temperature because of the dendritic morphology of the $FeZn_{13}$ (ζ) layer. A schematic diagram of the dross formation mechanism is shown in Figure 7. The Fe atoms react with Zn and small amounts of Al, resulting in the formation of dross particles such as $FeZn_{10}Al_x$ (δ).

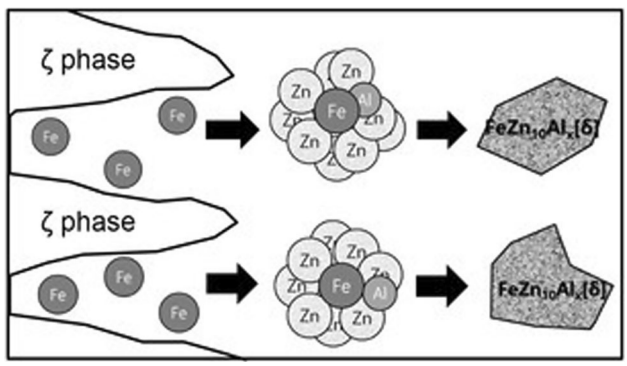

Fig. 7—Schematic diagram of the dross formation mechanism.

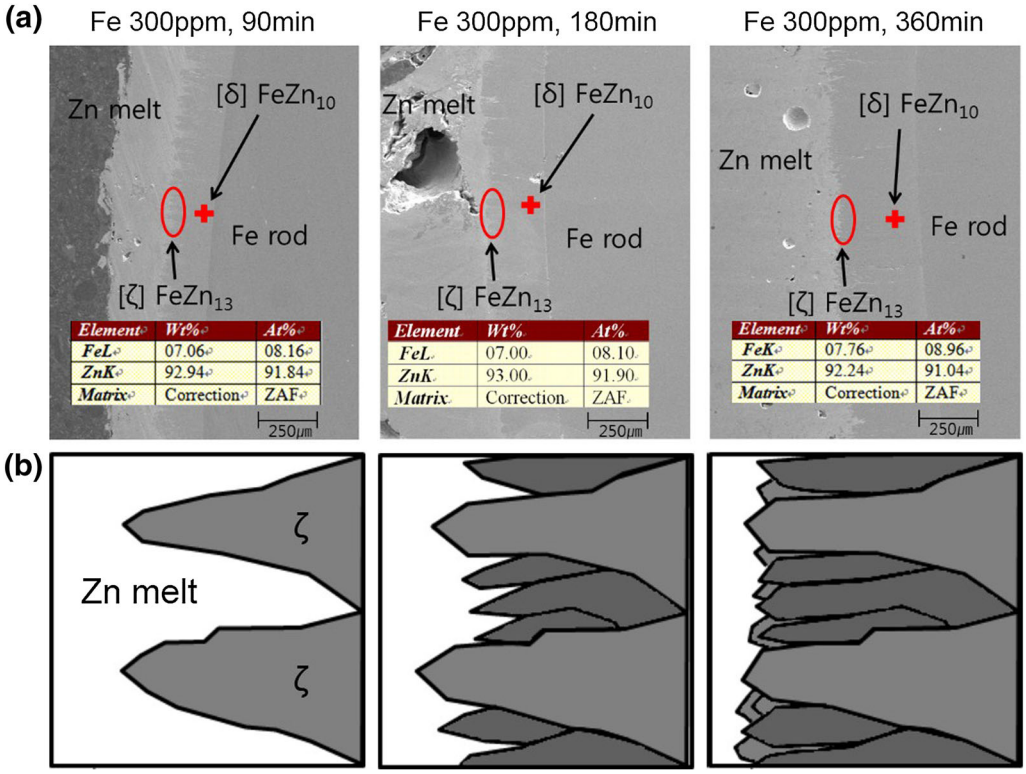

Fig. 8—(*a*) SEM image of the $FeZn_{10}$ (δ) and $FeZn_{13}$ (ζ) surface coating structure and (*b*) schematic diagram of the evolution process of the surface morphology as a function of time.

In Figure 2, the content of iron increased until 180 minutes, after which it remained constant in all conditions. In the experiments for the initial Fe content of 200, 240, and 300 mass ppm, the final Fe content in the molten zinc bath was 330, 340, and 450 mass ppm, respectively. As shown in Figure 8, the outermost dendrite-structured morphology densified and flattened with increasing rotating time. Thus, the densification of the $FeZn_{13}$ (ζ) layer reduces the supersaturation of iron in the boundary layer, resulting in the cessation of additional dissolution of iron. Nevertheless, since the total Fe increased over the solubility limit in the bulk liquid, it is necessary to quantitatively evaluate the number density of dross particles in the Zn bath.

D. *Effect of Initial Iron Content in a Zinc Bath on the Number Density of Dross Particles*

The phase diagram of the Zn-Fe-Al ternary system and experimental data are shown in Figure 9. Here, the phase diagram was calculated using FactSage^{TM}7.0, which is a commercial thermochemical computing software.[17,18] The initial points of the [Fe]° = 200 and 240 mass ppm conditions were located in the fully liquid phase, whereas the initial point of the [Fe]° = 300 mass ppm condition was located in the 'Liquid + δ' co-existing area. Thus, the δ phase dross initially exists in the latter condition. In the present study, all of the experimental points shifted to the 'Liquid + δ' area 180 minutes after the rotation started.

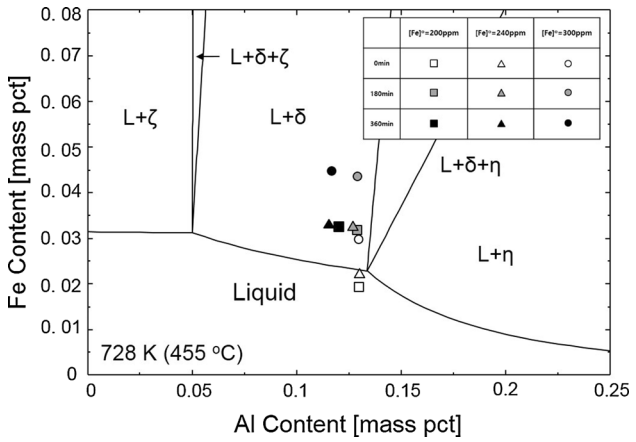

Fig. 9—Phase diagram of the Zn-Fe-Al system at 728 K (455 °C) and experimental compositions as a function of reaction time (phase diagram was calculated using FactSage^{TM}7.0).

SEM images of the dross particles (δ phase) are shown in Figure 10, which is in good correspondence to the phase diagram (Figure 9). This δ phase dross has a rectangular shape and contains a small amount of Al, which was also observed by Park *et al.*[5] and McDermid *et al.*[4] Because of a slight change in Al content with time as shown in Figures 2 and 9, only the δ phase dross was observed in the present study.

The size distribution and number of dross particles at different levels of the initial iron content in the 180

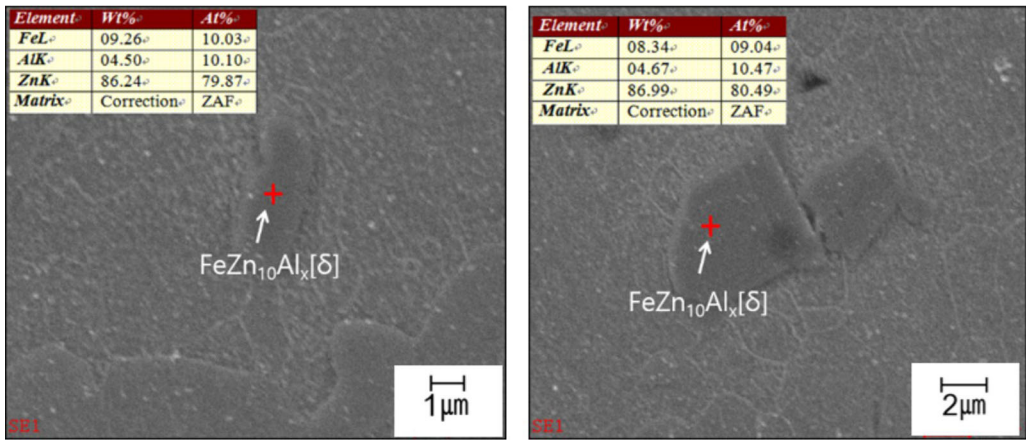

Fig. 10—SEM image of δ-phase dross particles in a molten zinc bath.

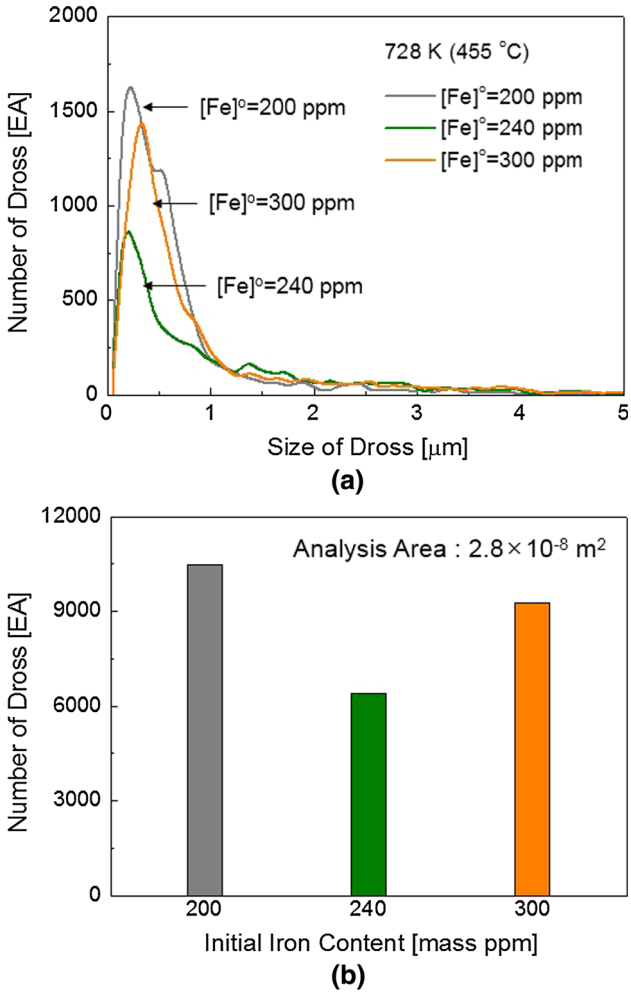

Fig. 11—(*a*) Size distribution and (*b*) number density of δ-phase dross particles at different levels of initial iron content in the zinc bath at 728 K (455 °C).

minutes samples are shown in Figure 11. The observation area *via* SEM was 2.8×10^{-8} m^2. Most of the dross particles were smaller than 1 μm, irrespective of the initial iron content. It is interesting that the number of dross particles was the smallest when the initial iron content in the zinc bath was 240 mass ppm, while it was nearly the same for the conditions with an initial iron content of 200 and 300 mass ppm. Consequently, the formation of dross particles can be reduced by minimizing the difference between the initial Fe content and saturation Fe content at a galvanizing temperature.

IV. CONCLUSIONS

The mechanism of iron dissolution as well as the effect of the initial Fe content in the Zn bath on the dissolution rate of iron was investigated using a finger rotating method (FRM) in which the iron cylinder was rotated with a fixed revolution per minute (rpm) to qualitatively simulate the dynamic galvanizing operation conditions. The major findings of the present study can be summarized as follows.

1. When the initial iron content in the zinc bath was 200 mass ppm, *i.e.*, [Fe]° = 200 mass ppm, the iron content in the zinc bath showed a rapid (0.71 ppm Fe/minute) increase, whereas a moderate (0.53 ppm Fe/minute) increase was observed when [Fe]° = 240 mass ppm. When [Fe]° = 200 and 240 mass ppm, the dissolution flux J was estimated to be 6.9×10^{-5} and 1.4×10^{-5} mol/m^{2}s, respectively. Because of a difference in driving force, the dissolution flux in the [Fe]° = 200 mass ppm melt was greater than that in the [Fe]° = 240 mass ppm melt [[Fe]$_{sat}$ = 250 ppm at 728 K (455 °C)].
2. The mass transfer coefficient of iron (k_M) in the present experimental condition was calculated as 1.2×10^{-5} m/s from Eisenberg's kinetic model, which was similar to the results derived by Giorgi *et al.* under industrial practice conditions.
3. The dissolution of iron occurred even when the initial iron content in the zinc bath ([Fe]° = 300 mass ppm) was greater than the saturation limit. This phenomenon was explained by the interfacial thermodynamics in conjunction with the morphology of the surface coating layer. By analyzing the SAED diffraction patterns using TEM, the outer-

most dendritic-structured coating layer was confirmed as monoclinic $FeZn_{13}$ (ζ). In order to satisfy the local equilibrium based on the Gibbs–Thomson equation, iron in the dendrite-structured phase spontaneously dissolved into the zinc bath, resulting in the enrichment of iron in front of the dendrite tip. Thus, iron dissolution occurred even though the initial iron content in the bulk zinc bath was already greater than the solubility limit at a given temperature because of the dendritic morphology of the $FeZn_{13}$ (ζ) layer.

4. Through the diffusion boundary layer in front of the dendritic-structured layer, dissolved Fe atoms diffused out and reacted with Zn and small amounts of Al, resulting in the formation of dross particles such as $FeZn_{10}Al_x$ (δ).
5. From the size distribution and number density of 'δ' dross particles at different levels of initial iron content, most of the dross particles were smaller than 1 μm, irrespective of the initial iron content. It was experimentally confirmed that the smaller difference between the initial iron content in the zinc bath and the iron solubility limit at a given temperature resulted in less dross particles being formed.

ACKNOWLEDGMENT

The authors express their appreciation to Professor YONGSUG CHUNG, Korea Polytechnic University, Korea, for his fruitful comment on the iron dissolution mechanism in zinc bath.

REFERENCES

1. N.Y. Tang and G.R. Adams: *The Physical Metallurgy of Zinc Coated Steel*, A.R. Marder, ed., TMS, Warrendale, PA, 1994, pp. 41–54.
2. A. Taniyama and M. Arai: *Mater. Trans.*, 2004, vol. 45, pp. 2482–85.
3. J. Nakano, D.V. Malakhov, S. Yamaguchi, and G.R. Purdy: *Calphad*, 2007, vol. 31, pp. 125–40.
4. J.R. McDermid, M.H. Kaye, and W.T. Thomson: *Metall. Mater. Trans. B*, 2007, vol. 38B, pp. 215–30.
5. J.H. Park, G.H. Park, D.J. Paik, Y. Huh, and M.H. Hong: *Metall. Mater. Trans. A*, 2012, vol. 43A, pp. 195–207.
6. M.L. Giorgi, J.B. Guillot, and R. Nicolle: *J. Mater. Sci.*, 2005, vol. 40, pp. 2263–68.
7. G.M. Michal, D.J. Paik, M.H. Hong and S.H. Park: *8th Int. Conf. on Zinc and Zinc Alloy Coated Sheet Steel* (*GALVATECH '11*), AIM, Genova, Italy, 2011.
8. Y.H. Liu and N.Y. Tang: *8th Int. Conf. on Zinc and Zinc Alloy Coated Sheet Steel Alloy Coated Sheet Steel* (*GALVATECH '11*), AIM, Genova, Italy, 2011.
9. P. Toussaint, L. Segers, R. Winand and M. Dubois: *4th Int. Conf. on Zinc and Zinc Alloy Coated Sheet Steel* (*GALVATECH '98*), ISIJ, Chiba, Japan, 2004.
10. N.Y. Tang: *Metall. Mater. Trans. A*, 1995, vol. 26A, pp. 1699–1704.
11. M.L. Giorgi, P. Durighello, R. Nicolle, and J.B. Guillot: *J. Mater. Sci.*, 2004, vol. 39, pp. 5803–08.
12. M.H. Hong, T. Kato, and K. Saka: *Tetsu-to-Hagane*, 1997, vol. 83, pp. 311–16.
13. D.R. Poirier and G.H. Geiger: *Transport Phenomena in Materials Processing*, TMS, 1998, p. 519.
14. M. Eisenberg, C.W. Tobias, and C.R. Wilke: *Chem. Eng. Prog. Symp. Ser.*, 1955, vol. 21 (16), p. 1.
15. A.R. Marder: *Prog. Mater. Sci.*, 2000, vol. 45, pp. 191–271.
16. S. Seetharaman: *Fundamentals of Metallurgy*, Woodhead Publishing Limited, 2005, pp. 250–57.
17. www.factsage.com (accessed July 2016).
18. C.W. Bale, E. Belisle, P. Chartrand, S.A. Decterov, G. Eriksson, K. Hack, I.H. Jung, Y.B. Kang, J. Melancon, A.D. Pelton, C. Robelin, and S. Petersen: *Calphad*, 2009, vol. 33, pp. 295–311.